

Chapter 7

Electrohydrodynamic Lithography of Functional Soft Materials for Advanced Applications

Pola Goldberg Oppenheimer

7.1 Introduction

A polymer is a chemical compound or mixture of compounds formed by polymerisation and consisting essentially of repeating structural units. The name is derived from the Greek, *πολυ*, *polu*, “many”; and *μέρος*, *meros*, “part”. DNA, proteins and starches in foods, the wheels on our skateboards, the tyres on our bikes and cars are all polymers. In fact, we are constantly surrounded by polymers wherever we may be. Thin polymer films on top of rigid or soft substrates have been investigated thoroughly during the last few years. Generally, instabilities in thin films are undesirable in nature and technology. Defect-free smooth films in the form of insulating layers or photoresists, e.g. coatings, lubricants or protective layers are essential for most important applications in the microelectronics industry. Liquid films are stable, unless an external destabilising force is applied at the surface, because of the minimisation of overall surface energy. The precise control of instabilities in films can however be utilised to produce novel structures by exploiting the destabilisation of an initially homogeneous layer for spontaneous structure formation process, and further decrease its length-scale to technologically interesting feature sizes. The capacity to construct nanostructures is essential for the development of functional devices that incorporate nanoscale features. The thin film instabilities can be generated either by intermolecular interactions, such as *van der Waals* forces (vdW), or by externally applied forces, e.g. electric fields or temperature gradients. Patterned thin polymer films have been implemented in applications ranging from molecular electronics [1–3] and optical devices [4–6], through bio-sensors [7, 8] to etching prevention [9].

P.G. Oppenheimer (✉)

School of Chemical Engineering, University of Birmingham, Edgbaston,
Birmingham B15 2TT, UK

e-mail: p.goldbergoppenheimer@bham.ac.uk

7.2 Surface Patterning via Electrohydrodynamic Instabilities

Intense interest in polymer patterning in the past decade originated from the diversity of the existing polymers, the relatively low cost, the convenient mechanical properties, and the compatibility of polymers with most patterning techniques. There are different bottom-up and top-down lithographic methods, such as photolithography, soft lithography imprinting, self-assembly of block copolymers, and instability-induced patterning. In an instability-driven approach to polymer patterning, application of a high (10^8 V/m) electric field across thin films at temperatures above the glass transition temperature of the polymer generates variations in charge density, destabilises the film and creates lateral, topographic features [10–13]. The emerging ordered patterns are a direct result of the interaction of a vertically applied electric field with a flow of fluid, i.e. it is named the electrohydrodynamic (EHD) patterning process. The physical principles that describe the deformation of a liquid surface induced by an electric field were first noted in 1897 [14], and were followed by the initial theories on the EHD instabilities [15, 16]. Ever since these ground-breaking studies, extensive investigations have been carried out on these issues [17–20].

Consider placing a liquefied insulator in a plate capacitor geometry and subsequently applying an electric field perpendicular to the film surface (Fig. 7.1). This causes an amplification of low amplitude capillary waves and EHD instabilities with a characteristic wavelength λ develop. First, the non-linear equation that governs the pattern formation process is formulated, followed by a simplified description in terms of a linear stability analysis leading to the derivation of a dispersion relation. At temperatures above the glass transition temperature (T_g), polymers can be described as incompressible viscous fluids. Given the geometry of a supported thin polymer film on a rigid substrate we can derive the equation of motion for this film.

For the typical experimental set-up schematically shown in Fig. 7.1, the natural choice is rectangular Cartesian coordinates. The y -coordinate of the film's interface is given by $h = h(x, t)$, where x is the lateral coordinate, t is the time and h is the film thickness.

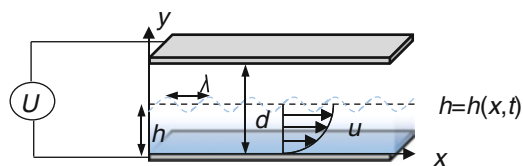


Fig. 7.1 Schematic geometry of a thin supported polymer film of thickness h . Temperature fluctuations induce surface waves with wavelength λ . The Poiseuille-type flow is indicated by a parabolic flow profile with velocity u

The *Navier–Stokes equation of motion* for an incompressible Newtonian fluid is:

$$\rho \left(\frac{\partial u}{\partial t} \right) + u \left(\frac{\partial u}{\partial x} \right) + v \left(\frac{\partial u}{\partial y} \right) + w \left(\frac{\partial u}{\partial z} \right) = - \frac{\partial p}{\partial x} + \eta \left(\frac{\partial^2 u}{\partial x^2} + \frac{\partial^2 u}{\partial y^2} + \frac{\partial^2 u}{\partial z^2} \right) + \rho g_x \quad (7.1)$$

The required *equation of continuity* is:

$$\frac{\partial u}{\partial x} + \frac{\partial v}{\partial y} + \frac{\partial w}{\partial z} = 0 \quad (7.2)$$

For flow in thin films, the N-S equation can be simplified in the following way:

1. High viscosities of the considered fluids result in a low flow velocity: the convective term in Navier–Stokes equation can be neglected \rightarrow

$$u \left(\frac{\partial u}{\partial x} \right) + v \left(\frac{\partial u}{\partial y} \right) + w \left(\frac{\partial u}{\partial z} \right) = 0$$

2. Slow dynamics: quasi-steady state is assumed for the system $\rightarrow \rho \left(\frac{\partial u}{\partial t} \right) = 0$

3. Thin-film geometry: gravity is negligible $\rightarrow \rho g_x = 0$

4. Flow in the film is in the x direction $\rightarrow v = w = 0 \rightarrow \frac{\partial u}{\partial x} = 0$ and the velocity dependent only on the y -coordinate.

Taking into account all the above considerations and substitution of the continuity equation leaves us with:

$$0 = - \frac{\partial p}{\partial x} + \eta \left(\frac{\partial^2 u}{\partial y^2} \right) \Rightarrow \frac{1}{\eta} \left(\frac{\partial p}{\partial x} \right) = \frac{\partial^2 u}{\partial y^2} \quad (7.3)$$

and

$$0 = \frac{\partial p}{\partial y} \quad (7.4)$$

meaning that the pressure p is uniform across the film's depth. Integration of this differential equation leads to a parabolic velocity profile:

$$u = \frac{1}{2\eta} \left(\frac{\partial p}{\partial x} \right) y^2 + c_1 y + c_2 \quad (7.5)$$

The *boundary conditions* are that the velocity is equal to zero at the solid interface and that there are no stresses at the interface:

1. $y = 0$; $u = 0$ (non-slip boundary condition)

2. $y = h$ $\sigma_{xy} = \eta \frac{\partial u}{\partial y} = 0$

Therefore, the constants that follow from the boundary conditions are:

$$c_1 = -2 \frac{\partial p}{\partial x} y|_{y=h} = -2 \frac{\partial p}{\partial x} h, \quad c_2 = 0$$

Substitution of which in Eq. (7.5) gives:

$$u = \frac{1}{2\eta} \left(\frac{\partial p}{\partial x} \right) y(y - 2h) \quad (7.6)$$

In the lubrication assumption, the lateral Poiseuille volume flow rate induced in the direction of decreasing pressure is obtained:

$$j_x = \int_0^h u dy = -\frac{1}{3\eta} \frac{\partial p}{\partial x} h^3 \quad (7.7)$$

The overall pressure is uniform all over the depth of the film. However, the pressure does depend on the film thickness, and its distribution at the film surface can be written as:

$$p = p_0 - \gamma \frac{\partial^2 h}{\partial x^2} + p_{el}(h) + p_{dis}(h) \quad (7.8)$$

where p_0 is the ambient air pressure, γ is the surface tension and the second term represents the Laplace pressure. For an applied voltage, U , the third term is the destabilising *electrostatic pressure* exerted on the interface by the interaction of the electric field, E_p , with the polarisation charges at the interface [21, 22] and given by:

$$p_{el} = -\epsilon_0 \epsilon_p (\epsilon_p - 1) E_p^2 = -\epsilon_0 \epsilon_p (\epsilon_p - 1) \frac{U^2}{[\epsilon_p d - (\epsilon_p - 1)h]^2} \quad (7.9)$$

where ϵ_0 is the dielectric permittivity of the vacuum, ϵ_p is the dielectric constant of the polymer and d is the capacitor plate spacing. The initial stage of structure formation is a sinusoidal undulation (Eq. 7.10) with an initial film thickness h_0 and low-amplitude undulation A

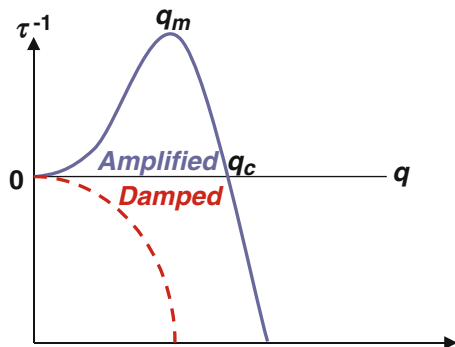
$$h(x, t) = h_0 + A e^{(iqx + t/\tau)} \quad (7.10)$$

The last term of the Eq. (7.8) is the disjoining pressure which is a result of the intermolecular forces exerted on the thin film [23] which plays a role in the near surface regions only. Due to a strong electric field generated in a capacitor device, only the electrostatic pressure and the Laplace term need to be taken into consideration.

A mass balance enforced by the continuity equation governs the equation for the air–polymer interface profile:

$$\frac{\partial h}{\partial t} + \frac{\partial}{\partial x} \left(\frac{h^3}{3\eta} \frac{\partial p}{\partial x} \right) = 0 \quad (7.11)$$

Fig. 7.2 Graphic representation of the dispersion relation (Eq. 7.12). While in the absence of or for a positive electrostatic pressure, all modes are damped ($\tau < 0$), the dispersion relation yields a dominant mode q_m with corresponding growth rate time τ_m^{-1} , for a negative p_{el}



A linear stability analysis [21, 24–26] leads to the establishment of the *dispersion relation* for the system relating the time constant τ with the wave vector q of a sinusoidal perturbation of the film:

$$\frac{1}{\tau} = -\frac{h_0^3}{3\eta} \left[\gamma q^4 + \frac{\partial p_{el}}{\partial h} q^2 \right] \quad (7.12)$$

The predictions are schematically shown in Fig. 7.2. While for $\frac{\partial p_{el}}{\partial h} \geq 0$, $\tau < 0$ for all q - fluctuations are damped, meaning that all growth rates are negative and the film is *stable*, for $\frac{\partial p_{el}}{\partial h} < 0$ all modes with $\tau > 0$ and $q < q_c = \sqrt{-\frac{1}{\gamma} \frac{\partial p_{el}}{\partial h}}$ are amplified and the film is *unstable*.

With time, the fastest mode of growth given by the maximum of Eq. (7.12):

$$q_m = \sqrt{\frac{1}{2\gamma} \frac{\partial p_{el}}{\partial h}} \quad (7.13)$$

will dominate, governing the most unstable wavelength of the system:

$$\begin{aligned} \lambda_m &= 2\pi \sqrt{\frac{2\gamma}{-\partial p_{el}/\partial h}} = 2\pi \sqrt{\frac{\gamma U}{\epsilon_0 \epsilon_p (\epsilon_p - 1)^2 E_p^{-3/2}}} \\ &= 2\pi \sqrt{\frac{\gamma [\epsilon_p d - (\epsilon_p - 1)h]^3}{\epsilon_0 \epsilon_p (\epsilon_p - 1)^2 U^2}} \end{aligned} \quad (7.14)$$

The associated maximal growth scales with the fourth power of the dominant growing wave vector, proportional to the surface tension and depending inversely on the viscosity for a given λ :

$$\frac{1}{\tau_m} = \frac{\gamma h_0^3}{3\eta} q_m^4 \quad (7.15)$$

As seen from Eq. (7.14), the theory suggests that a reduced feature size can be achieved by a thinner film, h , smaller plate spacing, d , lower surface tension and higher electric field.

The introduction of the reduced variables allows the superimposition of different experimental data sets. Defining characteristic variables of the instability:

$$\lambda_0 = 2\pi[\varepsilon_0\varepsilon_p(\varepsilon_p - 1)U^2]/\gamma \quad (7.16)$$

$$E_0 = 2\pi U/\lambda_0 \quad (7.17)$$

$$\tau_0 = 3\eta/h_0^3q_0^4 \quad (7.18)$$

Equation (7.14) can be written in simplified form:

$$\frac{\lambda}{\lambda_0} = \left(\frac{E_p}{E_0}\right)^{-3/2} \quad (7.19)$$

And Eq. (7.15) along with Eq. (7.18) provides the dependence of the time constant on the electric field:

$$\frac{\tau}{\tau_0} = \left(\frac{E_p}{E_0}\right)^{-6} \quad (7.20)$$

In which λ_0 is the characteristic wavelength, E_0 is the corresponding characteristic electric field and τ_0 is a characteristic time constant of the instability. As can be seen from Eqs. (7.16)–(7.20), the most unstable mode dependence on the electric field is $\lambda \propto E^{-3/2}$, characteristic time constant for the instability to set in has a very strong dependence on the electric field $\tau \propto E^{-6}$ and scales with the electrode spacing, d , to the sixth power ($\tau \propto d^6$). It also scales linearly with the film viscosity $\tau \propto \eta$. For a given film thickness, the characteristic lateral structure size exhibits a power-law dependence as a function of increasing electric fields, corresponding to a decrease in the electrode spacing.

To compare the destabilisation of materials with differing viscosities, it is useful to introduce an additional set of scaling relations. The inverse of the time constant defines a rate for the lateral displacement of material over a distance λ . Multiplied by η this defines a characteristic shear stress:

$$\sigma = \frac{\eta}{\tau} \quad (7.21)$$

Defining:

$$\sigma_0 = \frac{\eta}{\tau_0} \quad (7.22)$$

introduces the further scaling equation:

$$\frac{\sigma}{\sigma_0} = \left(\frac{E_p}{E_0} \right)^6 \quad (7.23)$$

7.2.1 EHD Patterning Under a Homogeneous Electric Field

The physical basis of the film instability can be understood by considering the competition of forces acting at the polymer–air interface. A polymer when heated above its glass transition temperature begins to flow as a viscous liquid. Subsequently, applying a voltage to the capacitor device (Fig. 7.3a) results in the development of an undulatory instability with a characteristic wavelength (Fig. 7.3b). The liquefied polymer experiences surface tension and gravity, which stabilise an initially homogeneous film, in contrast to the electrostatic pressure at the interface which destabilises the film. In the thin-film geometry, gravity is usually negligible and can therefore be disregarded.

For high electric fields, the destabilising electrostatic force overpowers the stabilising effects of surface tension acting at the film–air interface. With time, this force imbalance causes an amplification of film undulations induced by the electric field (Fig. 7.3b), until they span the capacitor gap, thus leading to rearrangement to the energetically favoured configuration of the liquid. It is characterised by monodispersed column diameters and a local hexagonal symmetry, which arises from the repulsion of wave maxima and minima, caused by the differing polarisation charges at these locations (Fig. 7.3c). The inter-column spacing is determined by the field strength and the polymer surface tension, and the column diameter is a function of the initial film thickness. Since the vertical liquid conformation (Fig. 7.3c) has lower electrostatic free energy than layered configurations (Fig. 7.3b), the electrostatic force drives the liquefied polymer to grow upward focusing the instability in the direction of the highest field.

Spacers of different height cause a gradual variation of the plate spacing, establishing a wedge geometry, in which the plate spacing varies by a few micrometres over a lateral distance of a few centimetres (Fig. 7.4). With a varying plate spacing in a lateral direction, the electric field varies as well. Since the characteristic time constant for the instability to set in has a very strong dependence on the electric field, $\tau \propto E^{-6}$ and scales with the electrode spacing, d , to the sixth power $\tau \propto d^6$, larger electrode spacing corresponds to a lower electric field. Therefore, for a given annealing time, different stages of instability can be observed on a single sample (Fig. 7.4, left). While in the wedge geometry, the spontaneous instability propagates towards decreasing confinement, the density and ordering of the columns increases (Fig. 7.4).

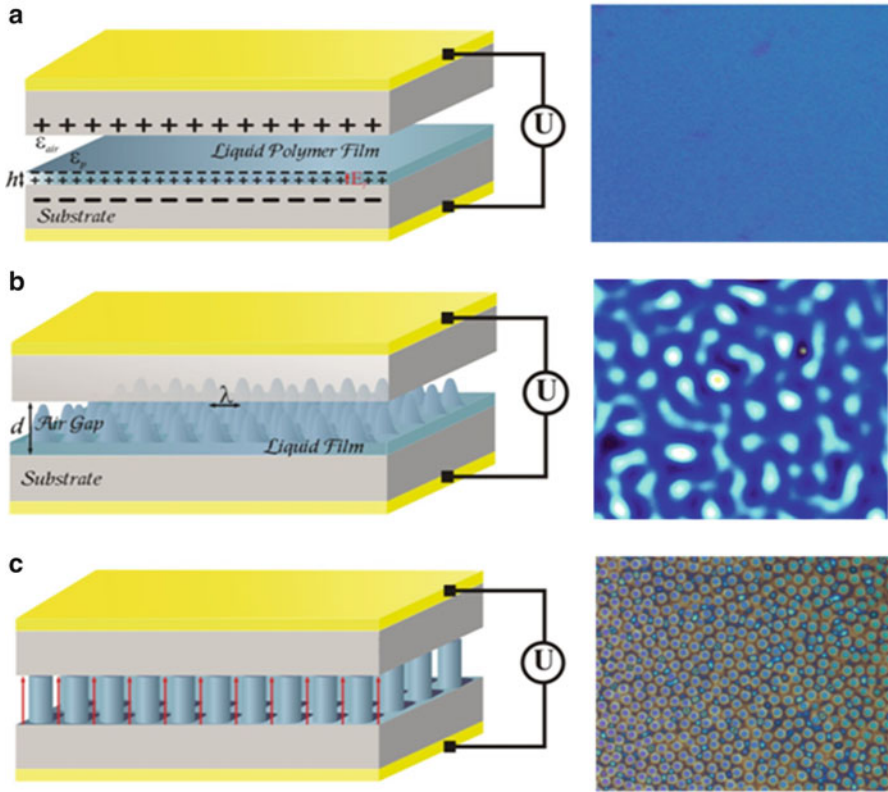


Fig. 7.3 Representative experimental set-up (*left*) with an evolving EHD instability of a polymer film under a laterally homogeneous electric field and the corresponding optical micrographs (OM) of the EHD pattern formation (*right*). (a) Applying a voltage through the capacitor assembly, results in the amplification of a surface undulation with a characteristic wavelength λ , which leads to the formation of hexagonally ordered columns (c). The origin of the destabilising electrostatic pressure is schematically shown in (b): the electric field causes the energetically unfavourable build-up of displacement charges at the dielectric interface (a), and in (c) the alignment of the dielectric interface parallel to the electric field lines lowers the electrostatic energy

7.2.2 Electrohydrodynamic Lithography

Substitution of the planar electrode by a topographically structured top plate (Fig. 7.5a) results in an inhomogeneous electric field, which focuses the instability towards the increased electric field, i.e. underneath the protruding structures, with an increased associated growth rate (recalling that $\tau \propto E^{-6} \propto d^6$, and therefore the polymer is destabilised first at the locations with the smallest d). Since $p_{el} \propto 1/d^2$ (Eq. 7.9) the electrostatic pressure is much stronger for smaller electrode distances, pattern replication of topographically structured upper electrode proceeds at a shorter time scale than the regular EHD structure formation.

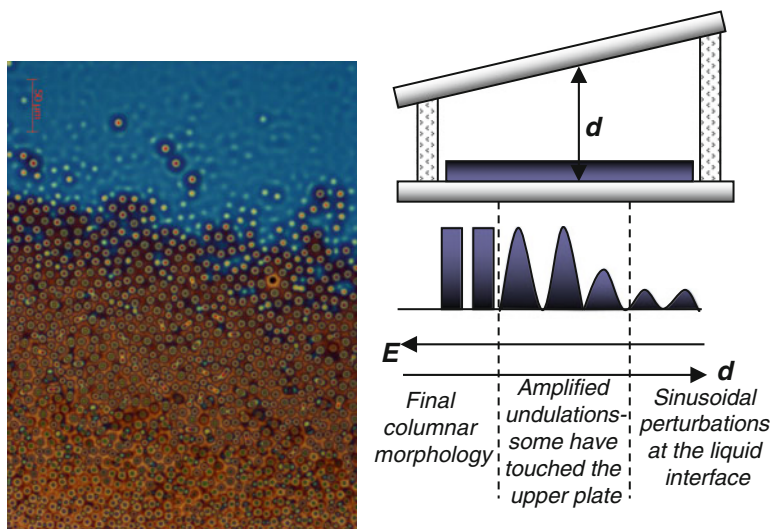


Fig. 7.4 *Left*: OM micrograph in which different stages of the instability are all present simultaneously. While on the top of the image undulations coexist with columns, the decreasing plate spacing towards the bottom increases the density of the columns, and thereby the inter-column interactions and ordering. *Right*: Largely exaggerated schematic representation of wedge geometry with the variation of the gap between the electrodes which cause the non-uniform strength of the electric field in the experiment and allows visualising the progress of the instabilities as they propagate from low to high field. Locally the configuration is nearly parallel

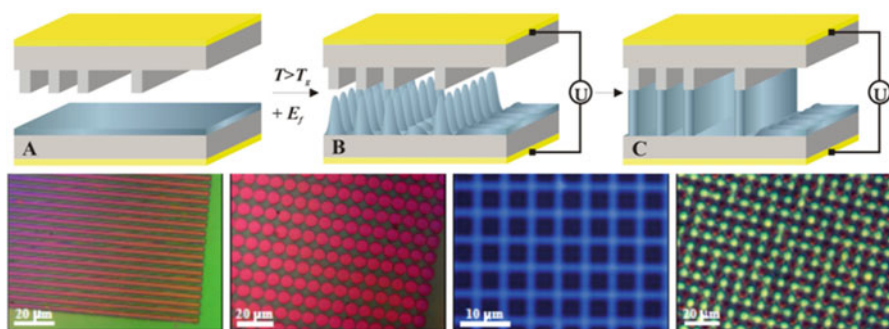


Fig. 7.5 *Top*: Schematic of experimental device during the EHD lithography process under a laterally heterogeneous electric field. (a) A structured upper plate creates a heterogeneous force field focusing the instability towards the protruding structures (b). In (c) a positive replica of the master pattern is transferred into the polymer. In unstructured regions, the film remains stable on a much longer time scale. *Bottom*: High fidelity EHD lithography showing the robustness of pattern replication with respect to the parameters of the electrode

The instability is guided towards the protruding patterns of the top mask, and the liquid polymer is drawn towards these protrusions. Consequently, the final structures are a positive replication of the master patterned electrode (Fig. 7.5). Pattern replication succeeds only if the length scale of the master pattern matches

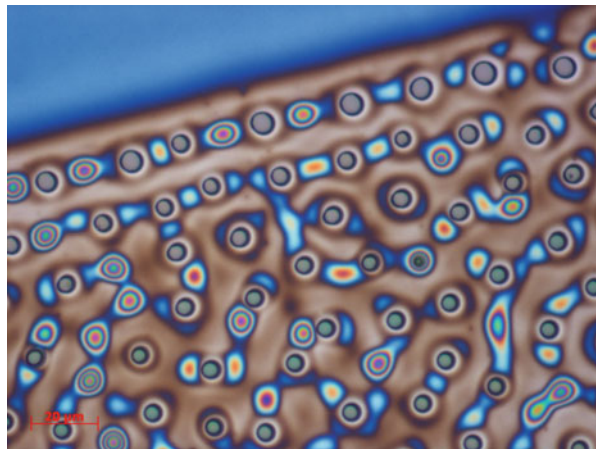
the instability wavelength. Using this electrostatic lithography process, varying structures can be replicated, ranging from lines, through circles and squares to letters and numbers.

7.3 Formation of Additional Instability Patterns

7.3.1 *Under a Featureless Mask: Nucleation and Viscous Fingering Instabilities*

When placing a featureless mask at a certain distance above the polystyrene film in a presumably laterally homogeneous electric field, additional intriguing patterns can be observed (Fig. 7.6). The image shows the nucleation effect at the edge of the film, which implies heterogeneity in the electric field, caused either by the edge of the upper electrode or by a dust particle. A strong lateral gradient in the electric field is induced from the presence of the edge, leading to the nucleation of the EHD instability along the edge [22]. However, instead of nucleated columns with a characteristic wavelength, λ , an alternating sequence of columns and wave maxima were observed: only every other maximum touches the upper electrode to form a pillar. This phenomenon was also previously observed by Schäffer et al. and was described as a competition between nucleation, depletion and the non-linearities in the system. A brief indication of the nucleation pathway is an initial amplification of a continuous rim parallel to the edge, which in turn breaks-up into waves eventually forming columns. The growth of the first column depletes its nearest neighbours, and the next nearest maximum is amplified first, being higher than the directly adjoining one. This chain effect propagates along the rim, and given enough time, all waves eventually will develop into columns.

Fig. 7.6 Optical micrograph of the nucleation of alternating columns and wave maxima induced by a straight edge



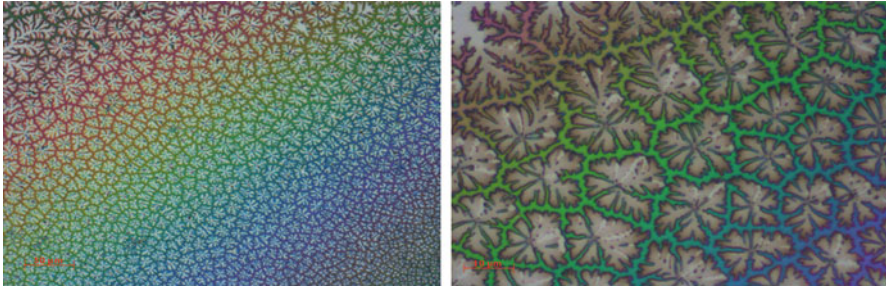


Fig. 7.7 Optical images of viscous fingers of trapped air appearing under the flat mask

When a fluid pushes a more viscous fluid into a very narrow gap between parallel plates, the interface between the two fluids develops an instability leading to the formation of finger-like patterns called viscous fingers (Fig. 7.7) [27]. Viscous fingering instability belonging to fractal geometry is a result of air trapped underneath the flat mask, which is the less viscous fluid driving the polymers melt. The physical source of this instability lies in the geometry of the moving interface [28].

7.3.2 Periodicity Mismatch Under Laterally Varying Electric Field

Imperfect replication of the template can occur however, in part of the lithography processes. These are explained based on the three replication cases which have been previously theoretically established [21] and experimentally observed [29]. In the presence of the laterally varying confinement (from d' to d), the liquid morphologies are organised according to the ratio of the plate spacing and the initial amount of polymer in the capacitor gap, i.e. the filling ratio, f ($f = h_0/d$). While the pattern selection during the early stage of the process is a sinusoidal surface undulation, for all samples, filling ratio establishes the late stage of pattern formation. The final morphology of the replicated pattern is determined by the partial coalescence of the initial pattern (Fig. 7.8). Since the shape of the generated pattern depends on the ratio of the intrinsic film undulation wavelength, λ_i , and the lateral periodicity of the master electrode, L_p , three replication mechanisms can be verified:

1. $\lambda_i \ll L_p$: *Periodicity mismatch-small wavelength regime*. The initial structure formation is followed by lateral coarsening of polymer material λ_i , leading to a partial positive replication.
2. $\lambda_i \approx L_p$: *Periodicity match-similar wavelength regime*. Perfect positive replica of the templates is obtained.
3. $\lambda_i \gg L_p$: *Periodicity mismatch-large wavelength regime*. The film pattern develops large number of defects and every protrusion of the electrode cannot produce a liquid column.

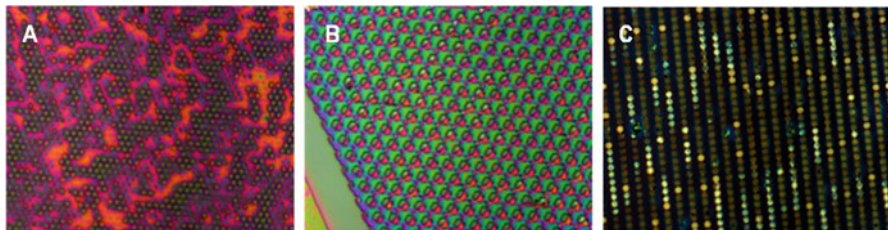


Fig. 7.8 A heterogeneous electric field is formed under the structured upper electrode, focusing the instability towards the protruding structures. (a–c) Optical microscopy images show rather imperfect replications of different structure of the electrodes under the periodicity mismatch conditions (e.g. in (a) $d = 500$ nm, $h/d' = 0.37$, $h = 83$ nm)

To obtain a faithful replication of the master topography, three criteria have to be fulfilled: (1) The filling ratio h/d' must be comparable to the surface area ratio, S (fraction of the template surface that protrudes towards the polymer film, $S = w/l_0$) of the topography, $h/d' \approx S$. (2) Periodicity match, $\lambda_i \approx L_p$ and, (3) The ratio of the interstitial spacing and the wavelength is smaller or equals to one.

7.4 Rapid EHD Patterning

While the origin of the underlying electrohydrodynamic (EHD) surface instabilities has long been established [14–16], its exploitation for high-throughput lithography is novel, and provides a way to replicate sub-micron scale patterns in a simple and robust fashion. One of the limiting aspects has, however, been the slow pattern-formation dynamics. Typical polymeric resists require prolonged-time span for the pattern formation to complete [30]. This is caused by the interplay of the factors that most resists consist of high molecular-weight (M_w) polymers which have a high melt viscosity in their accessible temperature window and the ability of accurate control over patterning onset and cessation. While too long annealing times result in coalescence of small-scale structures, which degrades pattern fidelity, too short an exposure to the electric field gives rise to an incomplete pattern replication. Since the electric field strength is limited by the dielectric strength of the materials in the narrow capacitor gap, the obtainable strain rates are generally low. Reducing the M_w of the resists typically leads to the reduction of the polymer's glass transition temperature, T_g , prerequisite the solidification above room-temperature.

A number of low-viscosity materials have been studied and exploited for fast EHD patterning, aiming to resolve the above intrinsic problems [31]. Different from the previously used polymers, the chosen materials had both a thermally accessible T_g as well as low viscosities upon softening, which resulted in a considerable reduction of the completion of the EHL to a few seconds only rather than hours, thus increasing the technological appeal of this technique. Low-viscosity epoxy materials were also studied by Dickey et al., who reported

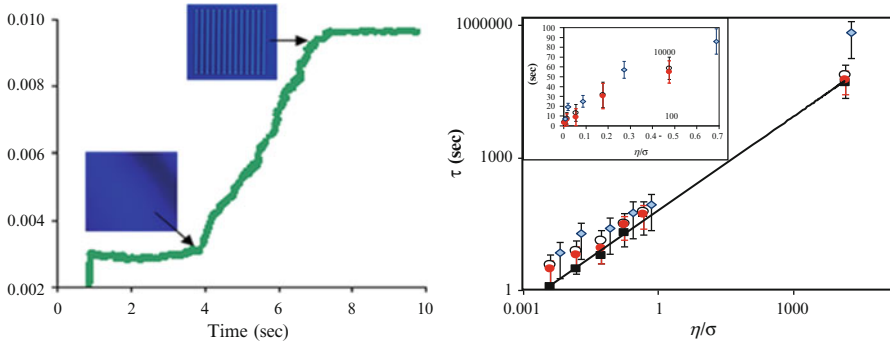


Fig. 7.9 (a) Overall-circuit current across capacitor devices versus time during the EHD patterning process. Ethyl Cellulose with $\eta = 0.084$ Pa s in a laterally varying electric field caused by a topographic grating ($h \approx 100$ nm, $d \approx 250$ nm (average), $U = 40$ V, and $T = 135$ °C). The insets show OMs of the sample at the various stages. (b). Variation of τ with viscosity in terms of Eq. (7.21). The data obtained by current monitoring (full red circles: $\tau = t_i$) agree within their error margins and are well described by the prediction of Eq. (7.21) (line). The data obtained from the termination times (diamonds, $\tau = t_f$) follow the same trend, but are offset towards longer times

similarly low patterning times [32]. A rapid EHD lithography, however, requires precise termination of the pattern formation process. While Dickey and co-workers achieve this by cross-linking of the resists, Goldberg Oppenheimer et al. demonstrated a method for the in-situ control of the EHL process during this short time span by monitoring the current across the patterning device [31]. Since the current is passed through the leaky dielectric once it spans the capacitor gap, the overall current is a good measure for electrohydrodynamic patterning completion.

Nevertheless, the acquired speed of the EHD instability requires an enhanced monitoring of the patterning process. Thus, minute but finite current that flows through the capacitor during pattern formation has been exploited. The current trace exhibits a sigmoidal shape that defines the characteristic onset and completion times of the EHD process (Fig. 7.9a). While t_i corresponds closely to the characteristic time of the instability τ , t_f indicates the completion of the pattern process.

To prevent a deterioration of the pattern by coarsening, it is essential that the sample is solidified at $t \approx t_f$. Because of the rapid patterning, quick sample quenching is essential. In situ optical investigation with a transparent electrode was thus exploited to correlate the structure formation process with the output current. Figure 7.9b shows the variation of the film destabilisation time with the viscosity of the polymer. To compare samples with different experimental parameters, the data is plotted as a function of η/σ , where all other experimental parameters are absorbed in the shear stress σ . While the optically detected onsets of the instabilities and of the current increase τ_i are well described by the prediction of Eq. (7.22), the completion of patterning τ_f is offset towards higher values compared

to the prediction of τ . To be noted that, despite the significantly more rapid patterning time, the EHD process is similar to that of high viscosity polymers and is therefore well described by a linear stability analysis.

7.5 EHD Patterning of Conductive Polymers

Since the total potential difference generated by the dipole layers at the interface is suppressed across the liquid layer, the driving force of the pattern formation in the case of a *leaky dielectric* polymer subjected to the EHL patterning lies in the electric field in the air gap, E^1 [25]. A sub-ambient pressure within the film balances the electrostatic force due to the field in the air gap on the polymer–air interface, placing the film in tension, and therefore generating the origin of the EHL instability.

For EHL patterning of conductive polymers however, free charges in the film (which substantially modify the electric field distribution in the film-air double layer) have to be taken into consideration. The following discussion is based on the formalism proposed by Pease and Russell [25] for charge-driven EHL patterning of leaky dielectric films.

p scales with the square of U

$$p = -\frac{1}{2} \frac{\varepsilon^g \varepsilon_0 U^2}{(d - h_0)} \quad (7.24)$$

with the gap fluid ε^g (which is an air gap in our case, i.e. $\varepsilon^g = \varepsilon_1$). The conductivity of the leaky dielectric suppresses the electric field in the film and the field in the gap drives the EHL pattern formation. This yields the dimensionless conductivity, Σ representing the ratio of a time scale for free charge conduction to the process time scale

$$\Sigma = \frac{\sigma \eta \gamma d^3}{(\varepsilon_1)^3 \varepsilon_0^3 U^4} \quad (7.25)$$

With the limit of $\Sigma \gg 1$ (in our study Σ is on the order of 10^7) the most dominant (characteristic) wavelength

$$\lambda = \frac{(2\sqrt{2})\pi}{U} \sqrt{\frac{\gamma(d - h_0)^3}{\varepsilon_0}} \quad (7.26)$$

is given by a force balance between the destabilising electrostatic pressure due to the field in the gap acting on the polymer–air interface with respect to the interfacial

height, h_0 and the γ acting to minimise the surface area, thus suppress the height variations. The characteristic time constant for the instability is given by

$$\tau = \frac{12\gamma\eta(d - h_0)^6}{U^4 h_0^3 \epsilon_0^2} \quad (7.27)$$

Despite the shorter destabilisation time and faster growing modes of a fully conducting polymer compared to a perfect dielectric, the patterning process is reminiscent of the well-studied case of generic polymers [33–35], thus confirming the same underlying physical mechanism.

To assess the electrolyte-gated field effect transistor (FET) performance, EHL-generated structure arrays were fabricated with gate length of 700 nm and pitch of 500 nm. Liquid-ion gate FET geometry was constructed using a potassium chloride (KCl) solution and a tungsten needle as a contacting electrode (Fig. 7.10a). The electrical drain current (I_{DS})-drain voltage (V_{DS}) characteristics of the device as a function of different gate voltages (V_G) are shown in Fig. 7.10b. Inset ii of Fig. 7.10b, presents the transfer characteristics at a constant drain-source voltage.

The positive gate voltages decrease the current and the values of I_{DS} increase upon raising the positive V_G at a negative V_{DS} indicating that the device exhibits p -type FET behaviour with the holes being the major charge carriers. Along with promising electrical transistor characteristics, the use of low-cost EHL lithographic technique and simple gate definition process steps could make such devices suitable candidates for next generation technology nodes.

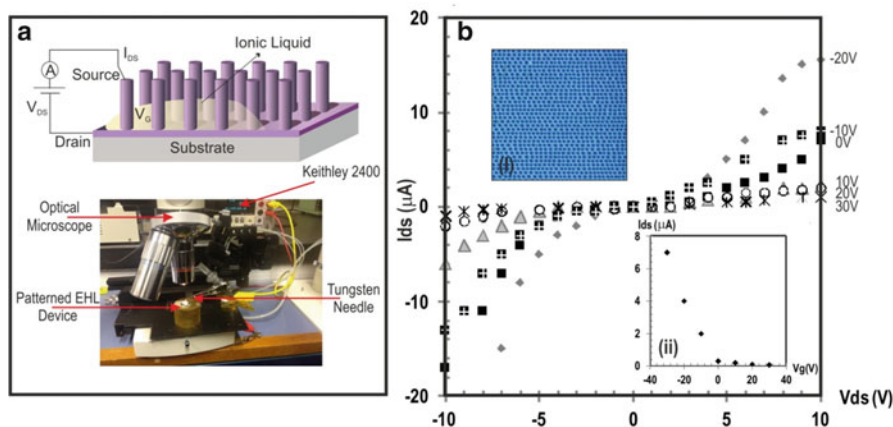


Fig. 7.10 FET performance of EHL-polypyrrole (PPY) architectures. (a) Schematic representation (top) and an overview image (bottom) of the configuration of a liquid-ion gate vertical FET using the EHL-generated structures on top of Si-SiO₂ substrate. A probe tip comprised of a tungsten needle was employed under a 1,000 \times magnification of an optical microscope to establish good connection between the source and the drain. (b). Drain current versus drain voltage characteristics of PPY electrolyte-gated transistor based on EHL fabricated pillars shown in a top-view optical image (inset b,i) and gate voltage performance (inset b, ii) of the PPY-FET described in (a)

7.6 EHD-Generated Architectures in Thin Polymer Films for Applications in Surface Enhanced Raman Scattering (SERS) and Solar Cell Devices

7.6.1 Hierarchical EHD Architectures as SERS Platforms

Using electrohydrodynamic instabilities, controlled self-organised hierarchical architectures can also be fabricated. Hierarchical electrohydrodynamic (HEHD) patterning uses a sequential instability in multilayer thin films caused by an applied electric field to guide the layered material to form designed structures in a one step process. Parameters can be altered to change the dimensions and the spacing of the structures during the HEHD patterning which are then covered in a plasmon-active-metal (in this case gold) to enhance the electromagnetic field for SERS applications. Using HEHD multi-scale three-dimensional structured arrays SERS substrates can be realised [35].

The structure formation in a multilayer thin-film assembly is controlled by carefully designing the layer sequence. In a polymer(*P1*)–polymer(*P2*)–polymer(*P3*)–air trilayer (Fig. 7.11), an uncontrolled dewetting of the multilayer is prevented allowing sequential destabilisation of the assembly layer by layer. The trilayer is assembled according to the T_g of the individual layers, starting from the highest for the bottom thin layer and the lowest for the top film, allowing each layer to be liquefied individually while preserving the underlying film in a stable state. The resulting hierarchical structures are an outcome of sequential electrostatic destabilisation. Since, the wetting properties of the three materials come also into play once the composite columns have formed, organising the resists according to the increasing surface tension stabilises the final coaxial architectures.

The various HEHD patterns show structure dependent SERS. For an optimised aspect ratio and geometry they give a 100-fold enhancement in SERS signals. Considering that each of the individual structures gives such high enhancements the HEHD patterned surfaces are a promising platform for multiplexed SERS detection. The demonstrated hierarchical structures open up a range of further possible implementations including for instance advanced photo-catalysis and bio-analytics.

7.6.2 Combined Bottom-Up and Top-Down Approach Based on EHD Formation of Surface Patterns in Thin Films

As depicted in Chap. 3, the ability to pattern functional polymers at different length scales is important for a range of applications and developments including the fabrication of micro plastic electronics, the production of optical components and bio-medicinal related research. EHD patterning can also be exploited for the fabrication of hierarchical functional patterns using electric field induced

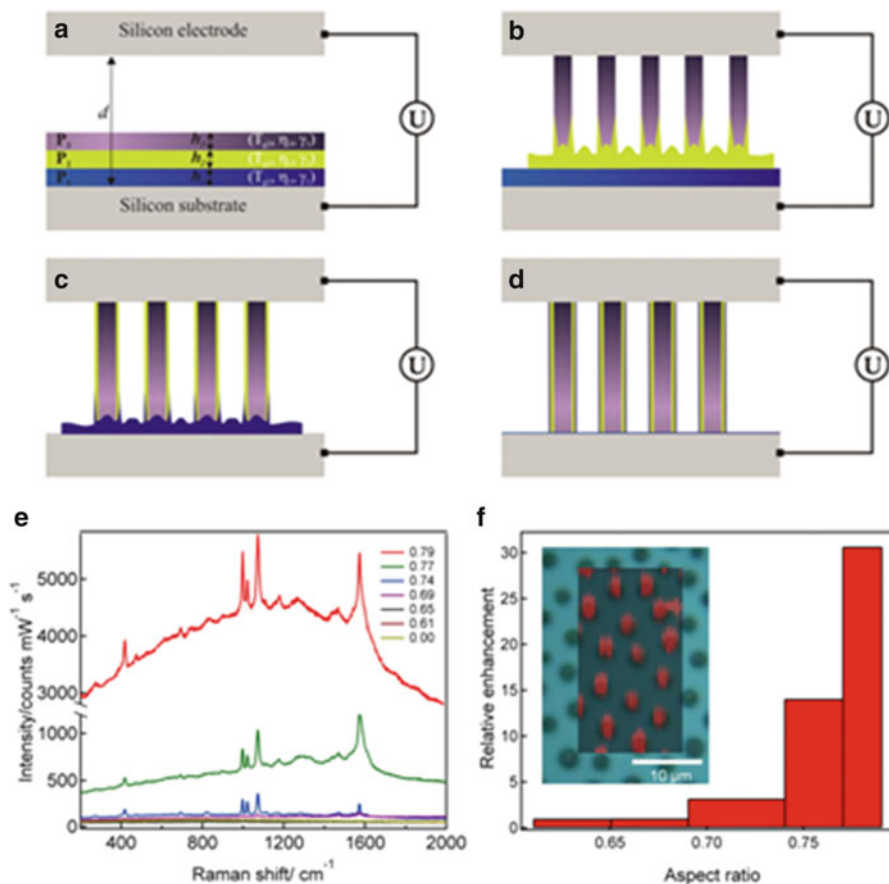


Fig. 7.11 Mechanism of the HEHD patterning process. **(a)** The initially assembled polymer trilayer is destabilised by applying a voltage. **(b)** The primary instability yields pillars which span the capacitor gap. The secondary instability arises from the deformation of the intermediate layer, P_2 occurring at the P_2 – P_3 contact line during the primary columns formation process. The amplification of the secondary instability guides the middle layer upwards forming a surrounding shell outside the primary pillar. **(c)** Subsequently, a third instability takes place at the bottom film and the liquified P_1 polymer is drawn upwards by the EHD torque while forming an additional mantle around the bilayer column. **(d)** The final configuration is comprised of a primary P_3 pillar, coated by additional concentric P_2 cylinder and the outer P_1 mantle. **(e)** SERS spectra of benzenethiol recorded from HEHD-generated substrates with pillars of various aspect ratios. **(f)** High aspect ratio structures show high SERS signals. The *inset* shows a SERS map over the optical image of a patterned area. The SERS signal for the 1,070 cm⁻¹ peak is in register with the column locations

instabilities to pattern a fully functionalised electron-conducting block copolymer [36]. This method combines the *bottom-up* self-assembly of block copolymer films (with internal structures on a scale of tens of nanometres) with the induced self-organisation of the intermolecular structure of the constituent crystalline blocks

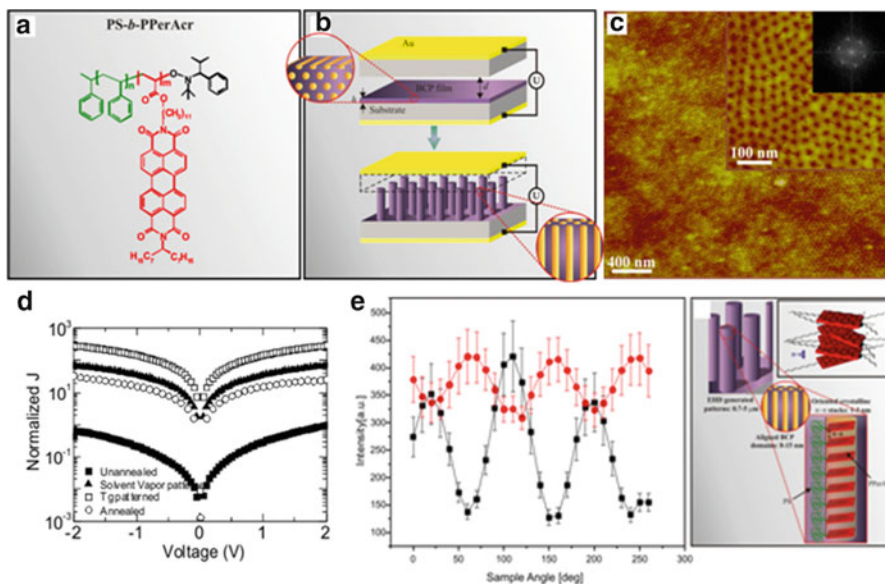


Fig. 7.12 (a) Molecular structure of the Polystyrene-block-poly(perylene bismide acrylate) (PS-b-PPerAcr) BCP comprised of an inert block of polystyrene and a crystalline side chain PPerAcr. (b) EHD patterning process with the zoomed-in schematics showing internal structure of the BCP film before (lying cylinder) and after patterning (vertical cylinders) process. (c) Representative AFM height image of the improved packing of cylinders with an average pore diameter of 14 ± 3 nm, formed inside PS-b PPerAcr matrix when swollen in chloroform vapour with 80 V applied across the capacitor electrodes for 5 h. The *inset* in (c) displays a FFT pattern of the structured film with a sixfold symmetry representing hexagonal packing of the cylindrical nano-domains. (d) J–V characteristics (DC) of ITO/BCP/ITO sandwiches non-annealed (*black squares*), EHD patterned using thermal annealing (*white squares*) and patterned in a solvent-vapour atmosphere (*black circles*) show improved charge transport properties in the patterned BCP films. (e) *Left*: Optical anisotropy analysis of internally oriented PS-b-PPerAcr patterns. Intensity dependence on the sample angle in a cross (*black squares*) and parallel (*red circles*) polarisation configuration. *Right*: Schematic image of the structural hierarchy

(in the range of 2–3 nm, Fig. 7.12e) inside the EHD driven microstructures, to produce functional patterns with a structural hierarchy. Such generation of structures which span several length scales is predominantly based on the interplay of molecular self-assembly and the structural control exerted by electrostatic forces. The polarisation of dielectric interfaces is the driving torque for the electrically induced copolymer domain orientation and the EHD guided instability. Block copolymer (BCP) microstructures also couple to the dielectric contrast between the different domains. The destabilising electrostatic pressure resulting from the electric field causes the energetically unfavourable build-up of displacement charges at the dielectric interface causing the alignment of the interface along the electric field lines, lowering the electrostatic energy. Amplification of the interfacial fluctuations caused by the interchange of the destabilising p_{ei} and the restoring γ gives rise to the pattern formation.

The micrometre-sized patterns contain an additional sub-nanostructure arising from the microphase-separated BCP morphology aligned parallel to the electric vector. Oriented nano-domains constitute the BCP crystalline stacks on the sub-10 nm scale with the π - π interactions oriented perpendicular to the E_f direction. These electro-conductive nano-domains within the pillars act as half-wave plate polarisers. The resulting morphology represents the optimal orientation of the copolymers nanostructure with respect to the substrate, exhibiting enhanced charge carrier percolation between the two electrodes (Fig. 7.12d). The charge transport across the entire device renders these aligned nano-morphologies technologically appealing for organic photovoltaic cells.

7.7 Concluding Remarks

In summary, the many interesting aspects of instabilities in thin liquid films are illustrated which are both of scientific and technological importance. While thin film instabilities are typically undesired in industrial and technological applications, they lead to novel surface morphologies and are applicable in alternative (soft-) lithographic techniques. In this context, EHD patterning exploits instabilities in softened thin films stemming from externally applied electrostatic forces to hydrodynamically generate topographic architectures with a controllable length scale in the technologically interesting sub-micrometre and sub-100 nm range. An externally applied field generates forces orders of magnitude larger than the electromagnetic fluctuations (long-ranged vdW forces) and the thermal vibrations (which are both comparatively weak), thus dominating film destabilisation. In such a limit, the EHD instability of a thin film is clearly attributed to the applied electric field and can be exploited as a lithographic technique. The advantages of this patterning technique are also noteworthy. The facile EHD patterning technique provides the ability for a straightforward design, manufacture and control of highly reliable and robust submicron patterns at low cost. Its versatility and the applications appeal are emphasised by the possibility of patterning a wide range of materials, single and multilayer film assemblies yielding varieties of hierarchical and anisotropic substructures. Therefore, the inclusion of the studied lithographic route into the advanced miniaturised devices manufacture processes can be envisioned.

Finally, EHD lithography is a versatile patterning tool on the sub-micrometre and nanometre length scales of functional materials. The aesthetic beauty of the generated structures, the applied technological potential and the underlying theories based on basic principles render this technique appealing, intriguing and set to become a pathway for advanced devices and applications.

References

1. Burn, P.L., Kraft, A., Baigent, D.R., Bradley, D.D.C., Brown, A.R., Friend, R.H., Gymer, R. W., Holmes, A.B., Jackson, R.W.: *J. Am. Chem. Soc.* **115**, 10117 (1993)
2. Dai, L.M., Griesser, H.J., Hong, X.Y., Mau, A.W.H., Spurling, T.H., Yang, Y.Y., White, J.W.: *Macromolecules* **29**, 282 (1996)
3. Nishizawa, M., Shibuya, M., Sawaguchi, T., Matsue, T., Uchida, I.: *J Phys Chem* **95**, 9042 (1991)
4. Burn, P.L., Holmes, A.B., Kraft, A., Bradley, D.D.C., Brown, A.R., Friend, R.H., Gymer, R.W.: *Nature* **356**, 47 (1992)
5. Healey, B.G., Foran, S.E., Walt, D.R.: *Science* **269**, 1078 (1995)
6. Xia, Y.N., Kim, E., Zhao, X.M., Rogers, J.A., Prentiss, M., Whitesides, G.M.: *Science* **273**, 347 (1996)
7. Liu, Y.L., Zhao, M.Q., Bergbreiter, D.E., Crooks, R.M.: *J. Am. Chem. Soc.* **119**, 8720 (1997)
8. Wells, M., Crooks, R.M.: *J. Am. Chem. Soc.* **118**, 3988 (1996)
9. Xia, Y.N., Mrksich, M., Kim, E., Whitesides, G.M.: *J. Am. Chem. Soc.* **117**, 9576 (1995)
10. Schaffer, E., Harkema, S., Roerdink, M., Blossey, R., Steiner, U.: *Macromolecules* **36**(5), 1645–1645 (2003)
11. Schaffer, E., Harkema, S., Roerdink, M., Blossey, R., Steiner, U.: *Adv. Mater.* **15**(6), 514 (2003)
12. Schaffer, E., Thurn-Albrecht, T., Russell, T.P., Steiner, U.: *Nature* **403**(6772), 874 (2000)
13. Schaffer, E., Thurn-Albrecht, T., Russell, T.P., Steiner, U.: *Europhys Lett* **53**(4), 518 (2001)
14. Swan, J.W.: *Proc R Soc* **62**, 38 (1897)
15. Frenkel, J.: *Phys. Z. Sowjetunion* **8**, 675 (1935)
16. Tonks, L.: *Phys. Rev.* **48**, 562 (1935)
17. Melcher, J.R.: *Phys. Fluids* **4**, 1348 (1961)
18. Melcher, J.R.: MIT Press, Cambridge, MA (1963)
19. Reynolds, M.: *Phys. Fluids* **8**, 161 (1965)
20. Taylor, G.I., McEwan, A.D.: *J Fluid Mech* **22**, 1 (1965)
21. Schaffer, E.: PhD thesis (2001)
22. Voicu, N.E., Harkema, S., Steiner, U.: *Adv. Funct. Mater.* **16**, 926 (2006)
23. Teletzke, G.F., Davis, H.T., Scriven, L.E.: *Rev Phys Appl* **23**, 989 (1988)
24. Wyart, F.B., Martin, P., Redon, C.: *Langmuir* **9**, 3682 (1993)
25. Pease, L.F., Russel, W.B.: *J Chem Phys* **118**, 3790 (2003)
26. Pease, L.F., Russel, W.B.: *Langmuir* **20**, 795 (2004)
27. Lindner, A., Coussot, P., Bonn, D.: *Phys. Rev. Lett.* **85**, 314 (2000)
28. Bensimon, D., Kadanoff, L.P., Liang, S.D., Shraiman, B.I., Tang, C.: *Rev. Mod. Phys.* **58**, 977 (1986)
29. Harkema, S.: PhD thesis (2006)
30. Leach, K.A., Lin, Z.Q., Russell, T.P.: *Macromolecules* **38**(11), 4868 (2005)
31. Goldberg Oppenheimer, P., Steiner, U.: *Small* **6**, 1248 (2010)
32. Dicke, M.D., Collister, E., Raines, A., Tsiartas, P., Holcombe, T., Sreenivasan, S.V., Bonnecaze, R.T., Willson, C.G.: *Chem. Mater.* **18**(8), 2043 (2006)
33. Harkema, S., Steiner, U.: *Adv. Funct. Mater.* **15**(12), 2016 (2005)
34. Morariu, M.D., et al.: *Nat. Mater.* **2**(1), 48 (2003)
35. Goldberg Oppenheimer, P., Mahajan, S., Steiner, U.: *Adv. Mater.* **24**(23), OP175 (2012)
36. Goldberg Oppenheimer, P., Kabra, D., Vignolini, S., Huttner, S., Sommer, M., Neumann, K., Thelakktat, M., Steiner, U.: *Chem. Mater.* **25**(7), 1063 (2013)